The Company of
Biologists

RESEARCH ARTICLE

FGFR2-activating mutations disrupt cell polarity to potentiate migration and invasion in endometrial cancer cell models

Samantha J. Stehbens[1,2,‡,§], Robert J. Ju[1,2,‡], Mark N. Adams[1], Samuel R. Perry[1,*], Nikolas K. Haass[2], David M. Bryant[3,4] and Pamela M. Pollock[1,§]

ABSTRACT

Fibroblast growth factor receptors (FGFRs) are a family of receptor tyrosine kinases that control a diverse range of biological processes during development and in adult tissues. We recently reported that somatic FGFR2 mutations are associated with shorter survival in endometrial cancer. However, little is known about how these FGFR2 mutations contribute to endometrial cancer metastasis. Here, we report that expression of the activating mutations FGFR2[N550K] and FGFR2[Y376C] in an endometrial cancer cell model induce Golgi fragmentation, and loss of polarity and directional migration. In mutant FGFR2-expressing cells, this was associated with an inability to polarise intracellular pools of FGFR2 towards the front of migrating cells. Such polarization defects were exacerbated in three-dimensional culture, where FGFR2 mutant cells were unable to form well-organised acini, instead undergoing exogenous ligand-independent invasion. Our findings uncover collective cell polarity and invasion as common targets of disease-associated FGFR2 mutations that lead to poor outcome in endometrial cancer patients.

KEY WORDS: FGFR, Endometrial cancer, Invasion, Migration, Polarity

INTRODUCTION

Fibroblast growth factor receptors (FGFRs) 1–4 are receptor tyrosine kinases (RTKs) (Baird et al., 1986; Turner and Grose, 2010). FGFR signalling plays a key role in mammalian embryogenesis, development and tissue homeostasis. Dysregulation of FGFR expression and signalling that can occur through genomic alterations are associated with pathological disease states, such as cancer (Babina and Turner, 2017; Dienstmann et al., 2014). Multiple members of this family are currently being pursued as cancer therapeutic targets.

We previously identified FGFR2-activating mutations in endometrial cancer (Pollock et al., 2007) that are associated with an increased risk of recurrence in a single institutional cohort (Byron

[1]School of Biomedical Sciences, Queensland University of Technology (QUT) located at the Translational Research Institute, Woolloongabba, Brisbane, QLD 4102, Australia. [2]The University of Queensland Diamantina Institute, Faculty of Medicine, The University of Queensland, Translational Research Institute, Woolloongabba, Brisbane, QLD 4102, Australia. [3]Cancer Research UK Beatson Institute, Glasgow, G61 1BD, UK. [4]Institute of Cancer Sciences, University of Glasgow, Glasgow, G12 8QQ, UK.
*Present Address: Institute for Molecular Bioscience, The University of Queensland, St. Lucia, Brisbane, QLD 4067, Australia.
[‡]These authors contributed equally to this work

[§]Authors for correspondence (s.stehbens@uq.edu.au; pamela.pollock@qut.edu.au)

S.J.S., 0000-0002-8145-2708

et al., 2012). Confirmatory studies in a multi-institutional cohort of over 950 endometrial cancer patients now show that FGFR2 mutations are associated with a decreased disease-free survival and decreased endometrial cancer-specific survival (Jeske et al., 2017). Endometrial cancer is the most common gynecologic malignancy in developed countries (SGO Clinical Practice Endometrial Cancer Working Group et al., 2014) with ∼76,000 deaths per year worldwide (Ferlay et al., 2015). Although 75% of endometrial cancers are detected early and have a good prognosis, patients who relapse post resection or present with metastatic disease have a very poor prognosis with a median survival of 7–12 months (Creutzberg et al., 2000). There is currently no treatment to cure patients with metastatic disease, highlighting the urgent need for new therapies (Longoria and Eskander, 2015; Temkin and Fleming, 2009). The majority of endometrial cancer-associated FGFR2 mutations are identical to germline activating mutations that result in developmental syndromes (Pollock et al., 2007). How these FGFR2 mutations function in the context of cancer is unknown. Here, we define the molecular mechanisms of two of the activating mutations we previously identified to be associated with recurrent disease and decreased survival, FGFR2[N550K] and FGFR2[Y376C].

All members of the FGFR family have a ligand-binding extracellular domain and a transmembrane domain, followed by a cytoplasmic kinase domain (Olsen et al., 2004). FGFR1–FGFR3 can undergo alternative splicing in the ligand-binding domain to give rise to alternative 'b' and 'c' isoforms that possess different ligand-binding specificities (Mohammadi et al., 2005; Ornitz and Itoh, 2001). For FGFR2, cells of an epithelial lineage typically express the 'b' isoform which binds FGF1, FGF3, FGF7, FGF10 and FGF22, ligands normally expressed by the underlying mesenchyme. Conversely, stroma typically expresses the alternative 'c' isoform, which responds to epithelium-derived FGF ligands. Consequently, this means that the local environment or stroma can signal to the adjacent epithelial structures and vice versa, a relationship that is often perturbed in invasive cancer (Dienstmann et al., 2014).

Classically, ligand-activated FGFR2 signals through signalling pathways including Ras–MAPK, PI3K–Akt, PLCγ, STAT and Src (Turner and Grose, 2010; Ornitz and Itoh, 2015), although the relative contribution of each pathway differs in different tissue contexts. The dogma for RTK signalling is that following activation, plasma membrane RTKs undergo receptor-mediated-endocytosis as a means of terminating cell surface signalling. However, it is now clear that receptors can continue to signal from endosomes following internalization (Jean et al., 2010; Villaseñor et al., 2016), enabling spatiotemporal signalling required for complex cellular functions such as cell migration. Previous studies of germline FGFR mutations indicate that point mutations in the receptor can result in differential localization and signalling (Citores et al., 2007; Harada et al., 2007; Lievens et al., 2004, 2006; Ahmed et al., 2008; Hatch et al., 2006). The mechanisms by which FGFR2

mutations initiate and/or drive endometrial cancer tumorigenesis and contribute to poor patient outcomes has not yet been identified.

In an effort to elucidate the biological consequence of FGFR2-activating mutations in endometrial cancer, we have established Ishikawa endometrial cancer cells expressing low levels of C-terminal eGFP-tagged wild-type (WT) and mutant FGFR2 (the epithelial 'b' isoform, hereafter referred to as FGFR2), FGFR2^{N550K} and FGFR2^{Y376C}, hereafter referred to as N550K and Y376C. Our rationale for studying these two activating mutations was two-fold; in comparison to the ligand-promiscuous mutation S252W, they are relatively understudied and although they are both considered to be activating mutations, this occurs through differing mechanisms. N550K, the second-most common FGFR2 mutation in endometrial cancer (Pollock et al., 2007), occurs in the kinase domain and is a key residue that forms part of the molecular brake region, which functions to restrict a conformational change to the active state (Chen et al., 2007; Byron et al., 2013). Y376C is a poorly characterised extracellular juxta-membrane mutation that introduces an extra cysteine residue that has been shown to facilitate disulfide-mediated receptor dimerization and activation in FGFR2 and FGFR3 (Adar et al., 2002; Byron et al., 2010; Robertson et al., 1998).

We report that expression of the activating mutations perturb polarization, migration and three-dimensional (3D) organization into acinar structures, ultimately leading to invasion. Mechanistically, we observe Golgi fragmentation and an inability of cells to reorient their intracellular pools of FGFR towards the leading edge, concomitant with a loss of directional migration during ligand-induced chemotaxis and chemokinesis. In a 3D acinus model, we observe an exogenous ligand-independent disruption of polarity concomitant with cells undergoing invasion into the extracellular matrix (ECM), which can be further potentiated by ligand (FGF10). Our findings suggest that the common target of FGFR-activating mutations in endometrial cancer is to disrupt the coordination of multicellular polarity, thereby priming cells for invasion. This study sheds light on the association of FGFR2 mutations with increased metastatic risk.

RESULTS
FGFR2-activating mutations exhibit aberrant receptor localization and signalling

To determine how FGFR2 activating mutations affect receptor function, we examined the spatio-temporal dynamics of eGFP-tagged WT FGFR2 and two activating mutations, N550K and Y376C, in Ishikawa endometrial cancer cells. To ensure there was no interference of C-terminal-binding partners, we included a linker region between the tag and the FGFR C-terminus (Mohammadi et al., 1991; Timsah et al., 2014; Lin et al., 2012). Ishikawa cells are a representative model of well-differentiated endometrial cancer; they express low levels of FGFR2, allowing us to examine the contribution of exogenous mutant expression, and show constitutive PI3K pathway activation due to a loss-of-function PTEN mutation. This genetic background makes them clinically relevant as most endometrial cancers with FGFR2 activation also carry loss-of-function PTEN mutations (Byron et al., 2008). As N550K occurs in the kinase domain and Y376C is an extracellular juxta-membrane, dimerizing mutation (Byron et al., 2010) (Fig. 1H; Fig. S1F), we hypothesized that, owing to potential conformational changes, their receptor spatio-temporal localization dynamics may differ, resulting in differential downstream signalling and cellular functions.

To ascertain whether the activating mutants localized differentially to WT protein, we examined receptor expression by live-cell spinning disc confocal (SDC) microscopy. In normal growth conditions (10% serum), WT FGFR2 localized to the cell membrane, as evidenced by an opaque surface fluorescence (Fig. 1A), in addition to a highly dynamic intracellular vesicular population (Movie 1). In contrast, both activating mutations had a pronounced intracellular pool (Fig. 1A and Fig. S1A) and led to an increase in the size of vesicular structures (Fig. 1B; mean size: WT, 0.42 μm^2; N550K, 0.62 μm^2; Y376C, 0.52 μm^2), with an increased number of vesicles also present in N550K cells (Fig. 1B; mean number: WT, 107; N550K, 165; Y376C, 133). These observations were supported by X-T kymographic analysis whereby diagonal tracks and vertical lines are indicative of dynamic and stationary vesicles, respectively (Fig. 1C). The WT receptor vesicles were more dynamic in contrast to the activating mutations, which was reflected in the quantitative analysis of vesicle trajectories over time (Fig. 1D). Membrane localization of activating mutant receptors was notably less in comparison to WT (Fig. 1A). To confirm the enhanced intracellular localization of mutant FGFR2, we next performed total internal reflection (TIRF) microscopy, which selectively illuminates proteins situated in close proximity to the plasma membrane (within ~100 nm) (Mattheyses et al., 2010) (Fig. 1E). Mutant FGFR2 was notably less at the cell surface in comparison to WT, which was confirmed by quantification of WT and mutant receptor integrated fluorescence intensity [Fig. 1F; mean TIRF fluorescence intensity in arbitrary units (a.u.): WT, 5859; N550K, 3099; Y376C, 2695]. We further supported the TIRF imaging approach, measuring surface receptor levels by selective-surface receptor labelling using an anti-FGFR2 antibody targeted to an N-terminal epitope in non-permeabilized conditions (Fig. S1B; ratio of surface to total mean: WT, 0.40; N550K, 0.31, Y376C, 0.23). These observations were also supported by cell surface biotinylation experiments on cells grown in 10% FBS. FGFR2 expression was assessed via western blotting of lysates generated by subcellular cell lysate fractionation and immunoprecipitation with streptavidin beads (Fig. S1C). A long exposure showed membrane localization of biotin-labelled WT FGFR2 but not mutant FGFR2 (boxed regions). These data suggest that in cells in serum, less mutant FGFR is present at the surface and it is predominantly intracellular.

We next examined whether FGFR activating mutants differentially regulated classical signalling pathways downstream of the receptor. We confirmed the exogenous expression levels of eGFP-tagged WT and mutant receptors by western blotting with antibodies against both the C- and N-terminal FGFR2 in addition to eGFP immunoblotting (Fig. 1G; Fig. S1D). A lower ~75 kDa band representing a cleaved form of FGFR2 was evident with a C-terminal antibody (C-17) as well as an antibody targeting eGFP (Fig. 1G). Endogenous levels of FGFR2 are low in the parental Ishikawa cell line and are almost undetectable in western blotting and immunofluorescence experiments allowing us to express FGFR–eGFP WT and mutations to levels observed in endometrial cancer cell lines that endogenously overexpress mutant FGFR2 (Taurin et al., 2018). Western blot analysis of cells grown in 10% serum revealed that expression of activating mutants resulted in a differential activation of downstream FGFR signalling pathways (Fig. 1G; Fig. S1D,E). Notably, expression of the N550K mutant resulted in increased phosphorylation of FGFR2, the FGFR-interacting protein FRS2α (at T436) and PLCγ-1 (at T783) (subunit encoded by *PLCG1*) in comparison to WT and Y376C, although PLCγ (T783) phosphorylation was also elevated for this latter mutant compared to WT. This indicates that although both mutants are activating, they may differ in their engagement of adaptor molecules and activation of downstream effectors. Together, with the live-cell imaging results, these data suggest that signalling may occur from intracellular compartments.
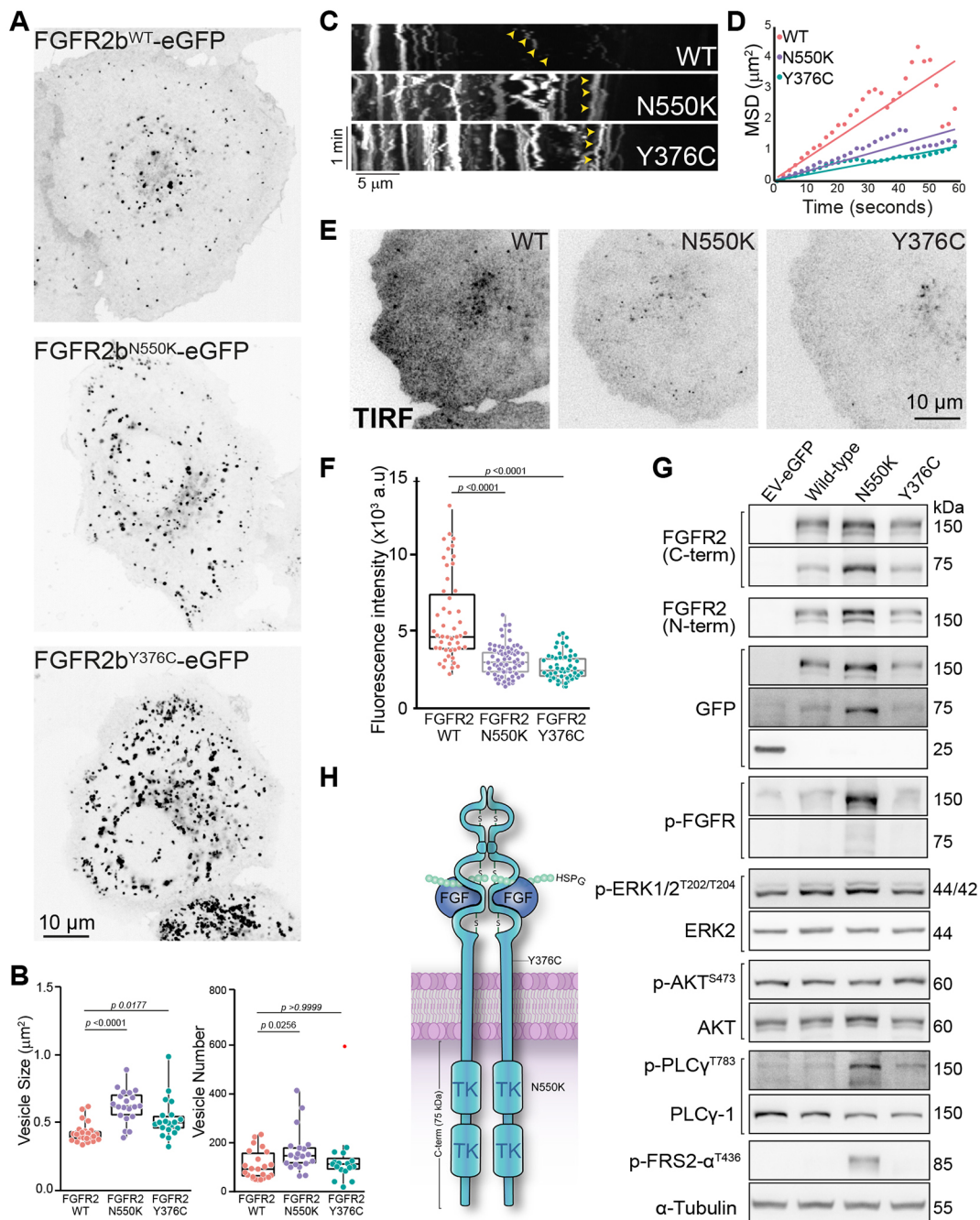
Fig. 1. FGFR2 mutations result in aberrant receptor localization and signalling. (A) Live-cell spinning disc confocal microscopy of Ishikawa cells stably expressing eGFP-tagged FGFR2 WT, Y376C or N550K. In this and subsequent figures, images are contrast inverted to better visualize receptor localization. (B) Analysis of average vesicle size and number, per cell (*n*). *n*=23 (WT), 20 (N550K), 20 (Y376C). Box-and-whisker plots show median, first and third quartile (box), and 95% confidence intervals (notches) with whiskers extending to the furthest observations within ±1.5 times the interquartile range. Dots are individual data points. *P*-values were calculated by a non-parametric Kruskal–Wallis analysis of variance with Dunn's multiple comparisons test correction and are displayed on graph. (C) Maximum intensity projection of *x-t* (time) kymographs of intracellular FGFR2 vesicular structures from cells in A. Static or pausing vesicles create vertical lines, dynamic vesicles create diagonal lines. Arrowheads identify a single vesicle track in each kymograph. (D) Averaged mean squared displacement plots of WT and mutant vesicle trajectories, as a function of time. (E) Representative TIRF microscopy images of WT and mutant FGFR-expressing cells. Excitation was at 488 nm. (F) Quantification of TIRF 488 nm fluorescence intensity, indicating that the mutant eGFP–FGFR2 variants have lower levels at the cell surface in comparison to WT. (G) Immunoblot of FGFR2 WT and N550K, Y376C mutant cell lines in normal growth conditions (10% FBS) probed for FGFR2 and proteins indicative of activated signalling pathways. Tubulin was used as a loading control. (H) Schematic of the FGFR2b surface dimer with the positions of mutations indicated. A detailed statistical summary for this and subsequent figures can be located in Table S2.

Ligand-dependent signalling differs in intensity and duration in FGFR-activating mutants

In order to investigate ligand-dependent signalling downstream of the activating mutants, we assessed whether mutant receptors could

be recruited to the cell surface when deprived of serum. We observed a progressive loss of the intracellular pool of the receptors in all cells during live-cell imaging of serum starvation, suggesting receptors were being recruited to the plasma membrane (Fig. S2A),

which was supported by cell surface biotinylation experiments (Fig. S2B). We readily observed cell surface recruitment with comparable membrane levels of WT and mutant FGFR2 in serum-starved conditions. We confirmed receptor surface recruitment by SDC time-lapse microscopy, where we analysed receptor internalization dynamics by stimulating serum-starved cells with FGF10 ligand (50 ng/ml), including heparin sulfate (5 µg/ml) to facilitate ligand binding and receptor dimerization. In WT cells, the opaque surface signal decreased over time (Fig. 2A), correlating with the appearance of vesicular structures (Fig. 2B), which coalesced towards the perinuclear receptor pool, becoming more predominant (Fig. 2C) as the surface receptor levels decreased. We observed similar phenomena in cells expressing mutant receptor, although the localization of the internalized receptor to the perinuclear pool and decreased rate of surface internalization was not as pronounced (Fig. S2C). These observations were supported by quantification of mutant receptor localization dynamics (Fig. 2D). These data suggest that the N550K and Y376C mutants can be recruited to the surface when serum deprived, and they exhibit differential receptor internalization dynamics when stimulated with ligand.

We next examined whether the differences in receptor internalization dynamics were reflected in FGFR2-dependent signalling pathways in response to ligand (Fig. 2E; 50 ng/ml FGF10, 5 µg/ml heparin sulfate, 0.5% FBS). Activation of FRS2α and PLCγ-1 by FGF10 was evident in WT transduced cells but not cells transduced with empty vector, confirming the phenotypic and signalling changes observed were mediated by exogenous FGFR2. Most notably, we observed alterations in the PLCγ pathway in cells expressing both mutants in comparison to WT. In N550K-expressing cells, we observed both a stronger and earlier induction of PLCγ-1^{T783} phosphorylation than in WT (Fig. 2E,F). In comparison, in Y376C-expressing cells the addition of FGF10 resulted in modest, but stable, induction of PLCγ-1^{T783} phosphorylation. Ishikawa cells do not possess mutations in any RAS family member (Weigelt et al., 2013), but do show constitutive activation of the MAPK pathway through an unidentified mechanism in serum-starved conditions (Fig. 2E, 0 min). Although ERK1 and ERK2 (ERK1/2, also known as MAPK3 and MAPK1, respectively) shows constitutive activation in cells transduced with empty vector (EV)-GFP, a further increase in ERK1/2 phosphorylation was seen following the addition of FGF10 in cells transduced with WT, and this increased phosphorylation was sustained over a longer period of time in cells expressing the activating mutations.

To investigate the phenotypic output of signalling downstream of the activating mutations, we measured cell proliferation using total protein levels in combination with live-cell microscopy studies. Expression of the activating mutations resulted in an increase in proliferation, independent of ligand (Fig. 2G). Unexpectedly, the addition of ligand to WT-, N550K- or Y376C-expressing cells resulted in decreased proliferation. To further clarify this effect, we examined the cells by live-cell imaging over 6 days (Movie 2). In WT cells, we observed an induction of cell migration with the addition of ligand, with cells losing their epithelial cobblestone appearance, moving away from cell islands to move as single cells. In cells expressing N550K, this migratory phenotype was present in unstimulated conditions and slightly enhanced with ligand. In contrast, in cells expressing Y376C, we observed two populations, one with an enhanced migration of individual cells and another with an aberrant growth pattern whereby cells grew in tightly clustered islands. This suggests that stimulation of FGFR-dependent

signalling induces a switch from proliferation to a pro-migratory phenotype in endometrial cancer.

FGFR-activating mutants are not sequestered in the endoplasmic reticulum
Previous studies of dimerizing mutants in other FGFR family members have reported that mutant receptors are retained in the endoplasmic reticulum (ER) or Golgi en route to the cell surface (Hatch et al., 2006) (reviewed in Foldynova-Trantirkova et al., 2012). To test whether the enriched receptor endosomal pool was due to Golgi retention, we examined the localization of eGFP-tagged receptors relative to the Golgi marker GM130 (also known as GOLGA2) through immunofluorescence in full growth medium (10% FBS). Whereas the perinuclear pool of receptors localized in close proximity to the Golgi (Fig. 3A), there was limited overlap, indicating that the receptor was unlikely to be sequestered in the Golgi. Interestingly, we observed fragmentation of the Golgi in cells expressing activating mutants. As the fixation required for immunofluorescence destroys the ER reticular structure and potentially the antigen epitope, resulting in diffuse ER/calnexin staining (Melan and Sluder, 1992; Schnell et al., 2012; Bhattacharyya et al., 2010) (Fig. S3A), we visualized the ER through live imaging of cells co-expressing the ER marker mCherry–Sec61. We observed vesicular FGFR2 directly adjacent to mCherry-Sec61 reticular structures, which extended to the cell periphery (Fig. 3B,C). To explore both of these observations further we examined mutant receptor spatio-temporal dynamics in cells co-expressing a mCherry-labelled marker for the Golgi (Rab6a; Fig. 3D,E, Movie 3) and ER (Sec61; Fig. 3B,C, Movie 4) using live-cell SDC microscopy. Vesicular FGFR2 structures of both WT and mutant FGFR2 moved unhindered, independently of any obvious retention in either Golgi or ER structures. This indicates that FGFR2-activating mutants are not retained in the ER or Golgi. In order to identify the intracellular compartment that receptors were localizing to, we examined a panel of classic endosomal and lysosomal compartment markers by immunofluorescence, including those for recycling endosomes (Rab11), the ER-Golgi compartment (ERGIC53, also known as LMAN1), lysosomal markers (Lamp1, Lysotracker) and markers for late endosomes (Rab7). Surprisingly, we observed no apparent differential endosomal localization of either of the FGFR mutants in comparison to WT receptors (Fig. S3B–F). Although the caveat remains that mutant FGFRs may localise to an unidentified endosomal pool, our data suggest that the differential signalling we observe is not due to altered trafficking routes of the FGFR mutants per se, but rather is due to enhanced localization to the classical endocytic route for FGFR2 combined with constitutively active receptor signalling from these compartments. This concept is similar to activating mutants reported for the HGF receptor c-Met (Ménard et al., 2014; Barrow-McGee and Kermorgant, 2014).

Expression of FGFR-activating mutants results in fragmentation of the Golgi apparatus
As Golgi integrity and polarization towards the leading edge of cells is typically involved in persistent migration in one direction ('productive migration') (Kupfer et al., 1987; Etienne-Manneville, 2004; Miller et al., 2009), we next addressed the role of Golgi organization in mutant-expressing cells. Expression of activating mutants resulted in a ~30–50% increase in the angle (Fig. 4A,B; mean: N550K, 147°; Y376C, 172°) of Golgi dispersion in comparison to WT (116°). To test for the impact of these changes on migration, we imaged cells expressing WT or mutant receptors

Fig. 2. See next page for legend.

Fig. 2. Ligand-dependent internalization and signalling of FGFR2 WT and activating mutants in Ishikawa cells. (A) Spinning disc confocal microscopy of eGFP-tagged FGFR2 WT receptor internalization dynamics in response to FGF10 ligand stimulation. Ishikawa cell stably expressing eGFP-labelled WT FGFR2 receptor (cyan) that were serum starved (90 min; 0.5% FBS, $t0$), prior to the addition of ligand (50 ng/ml FGF10, 5 μg/ml heparin). The ROI1 (yellow) indicates the area for the total or surface receptor, the ROI2 (white) indicates the area of the perinuclear receptor pool. Time is in minutes. (B) Time-lapse images of outlined boxed area in A demonstrating receptor internalization as visualized by a loss of opaque surface fluorescence, and an increase in vesicular structures which coalesce and accumulate in the perinuclear pool. (C) Time-lapse images of perinuclear receptor accumulation from A, demonstrating an increase in receptor fluorescence intensity over time. Intensity values are inverted and image is scaled to 50% for display purposes to prevent saturation of vesicular structures. Hoechst 33342 (magenta) labels the nucleus in A–C. (D) Quantification of receptor internalization dynamics of eGFP-labelled WT and mutant FGFR2. Fluorescence intensity profiles measured as a function of time were normalized to the $t0$ intensity for each ROI outlined in A ($n{\geq}10$ cells per condition). The solid line is the average intensity of all ROIs and dashed lines are 95% confidence intervals. The surface receptor fluorescence decreases in response to ligand (ROI1, blue line), whereas the perinuclear receptor fluorescence (ROI2, grey line) intensity plots exhibit variable dynamics over time in response to ligand. (E) Immunoblots of Ishikawa cells stably overexpressing eGFP-tagged FGFR2 WT and activating mutants N550K and Y376C stimulated with FGF10. In brief, cells were serum starved (0.5% FBS) overnight prior to ligand stimulation (50 ng/ml FGF10, 5 μg/ml heparin). At the indicated time points (0–16 h), cells were lysed and collected for western blot analysis. Specific antibodies detecting total and phosphorylated proteins that are indicative of activated downstream signalling pathways were used. Tubulin was used as a loading control. The blot presented is a representative example of three independent experiments. (F) Quantification of PLCγ and FRS2α signalling from three independent experiments. The signal for phosphorylated protein was divided by the signal for total protein for PLCγ and FRS2α, and normalized to the value for the loading control protein (α-tubulin). Time course values were normalized to $t0$ (starved) values. Error bars are s.d. (G) Quantification of cell proliferation as measured by the whole-protein content fold increase (day 4 to day 0), normalized to that in empty vector control cells. Cells were grown in 2% FBS with 5 μg/ml heparin in the presence or absence of FGF10 (50 ng/ml); n=3 technical triplicates performed on two independent occasions. Graph is mean±s.d. Representative frames from phase contrast time-lapse imaging of Ishikawa cells stably expressing FGFR2 WT or N550K and Y376C, grown for 6 days are shown underneath. Cells were grown in 2% FBS with 5 μg/ml heparin in the presence or absence of FGF10 (50 ng/ml). Scale bar: 20 μm. Cells are colour highlighted to allow visualization of the cell morphology.

by time-lapse epifluorescence microscopy during wound closure in the presence and absence of FGF10 ligand stimulation. We co-expressed mCherry empty vector in all conditions to generate high-contrast images to facilitate cell tracking. We observed that cells expressing WT FGFR2 were able to close the wound within 24 h, with leading edge cells moving in a coordinated manner (Fig. 4C–E). In contrast, cells expressing activating mutations exhibited erratic migration dynamics, with cells often breaking free from the leading edge and individually migrating in and out of the wound, resulting in failure to close the wound (Movie 5). This suggested that the perturbation of Golgi polarization observed in activating mutants resulted in the loss of polarized migration.

FGFR-activating mutants exhibit a loss of directional persistence during two-dimensional migration

As our data indicate that FGFR2-activating mutations induce a migration polarization defect, we examined the ability of cells to respond to an FGF chemotactic gradient (Fig. 5A). We quantified four migration parameters to describe migration behaviour: total track length; displacement, the shortest distance between the initial and final points; persistence, a ratio of cell displacement to distance

migrated and speed (see the Materials and Methods for formula details). In the absence of ligand, WT and N550K cells exhibited limited intrinsic migration, often oscillating in place. In contrast, Y376C cells showed significantly longer total track lengths, displacement and speed supporting the constitutive activation of this mutant receptor (Fig. 5B–E). In the presence of a FGF10 gradient, WT cells migrated persistently towards the gradient, a behaviour not observed in cells expressing mutant FGFR2. Instead, mutant cells exhibited an increase in tortuosity, randomly switching direction throughout the time-lapse sequence, seemingly unable to detect the ligand-gradient, an observation that was substantiated by migration track plots and the loss of directionality (Fig. 5A,D; persistence). In WT cells, the increase in track length observed with the addition of ligand correlated with an increase in migration speed and productive migration towards the ligand gradient. The increase in migration in response to ligand observed in the cells expressing WT receptor was not seen in cells expressing mutant receptor. We observed similar findings in chemokinesis assays (Fig. S4). Collectively, our data demonstrate that the fragmented Golgi observed in mutant cells is concomitant with a strong defect in polarity and directional migration.

To elucidate how the migration phenotype of mutant cells resulted in non-productive migration, we examined cells co-expressing the filamentous actin reporter mCherry–Lifeact by time-lapse SDC microscopy (Riedl et al., 2008) (Movie 6). Live-cell imaging revealed that WT cells stimulated with FGF10 were able to undergo polarized migration, forming a broad fan-like, leading-edge lamellipodia with a trailing rear (Fig. 5F). N550K mutant cells appeared unable to polarize and instead extended and retracted multiple lamellipodial extensions in a seemingly random manner (Fig. 5G,H).

As (1) mutant FGFRs were predominantly intracellular in serum-containing conditions (Fig. 1), and (2) these could be recruited to the PM upon serum withdrawal (Fig. 2), and (3) that the Golgi and MTOC orient towards chemotactic gradients, we reasoned that the intracellular pools of FGFR2 may similarly need to polarize towards the leading edge of cells. To this end, we observed that the perinuclear pool of receptor oriented towards the migrating front of WT cells. In stark contrast, mutant cells exhibited a dispersed perinuclear receptor pool with no clear orientation (Fig. 5F,G; Movie 7). Taken together, this demonstrates that activating mutations in FGFR2 result in a loss of front–rear polarity, concomitant with an inability to organize the endosomal pool of FGFR, and a decrease in polarized migration in both 2D chemotactic and chemokinesis assays.

FGFR-activating mutations differentially effect endometrial acinar morphogenesis and 3D invasive migration

A common feature of tumorigenesis is the progressive loss of tissue architecture (Halaoui et al., 2017), which in healthy tissue requires the collective coordination of individual polarity of each cell. We reasoned that mutant FGFRs should therefore display a defect in multicellular polarization. We generated acini expressing WT and activating mutants of FGFR by adapting the well-established Matrigel™ overlay assay (Bryant and Mostov, 2008; Debnath and Brugge, 2005; Lee et al., 2007). In brief, acini were grown for 8 days from a single-cell that proliferates and assembles into a polarized spherical monolayer with a central lumen, a structure that is dictated by a compliant ECM (Matrigel™). Empty vector control and WT receptor-expressing acini formed well-polarized structures with the Golgi oriented towards the apical lumen and the basement membrane marker β4-integrin (ITGB4) demarcating the basal
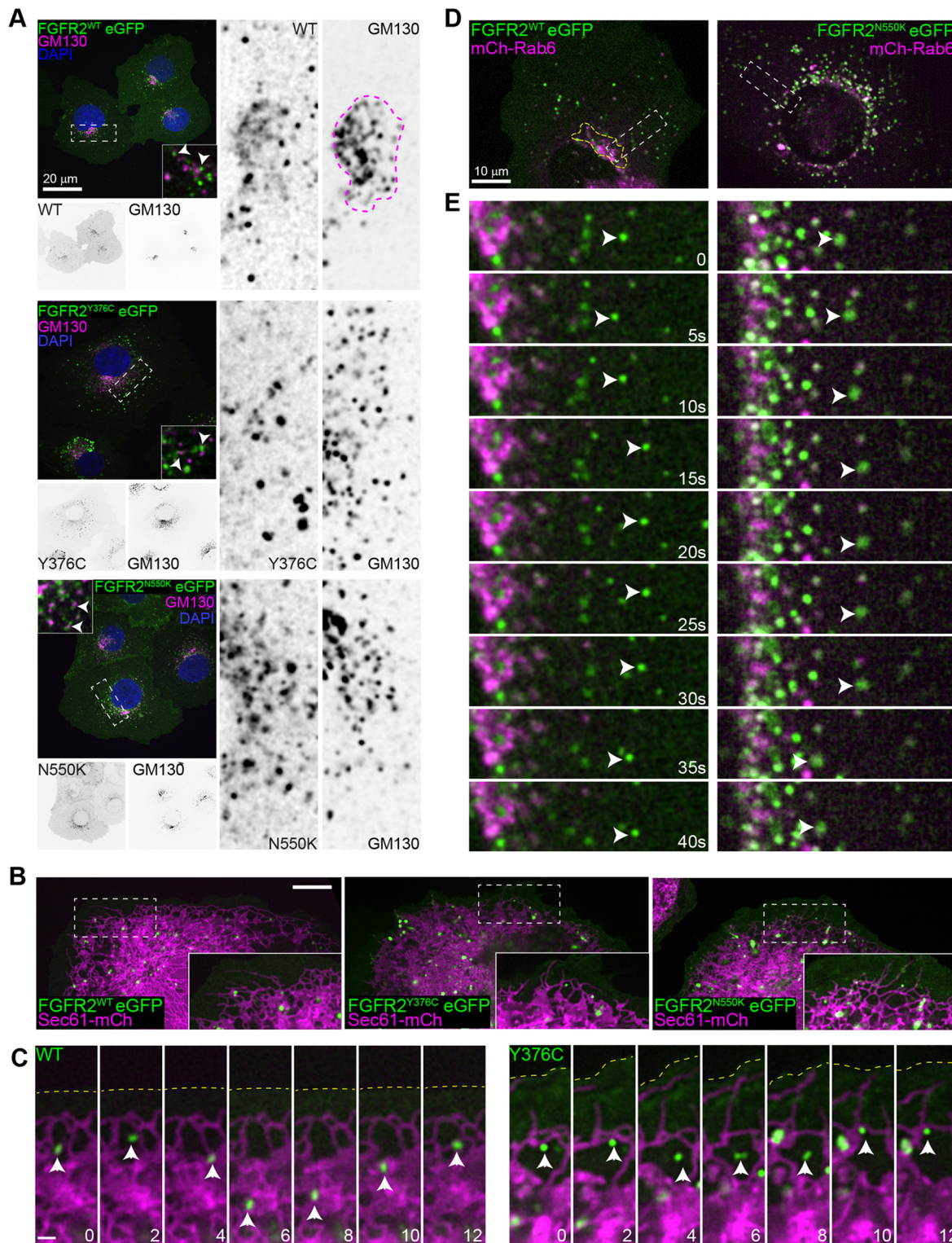
Fig. 3. FGFR mutants are not sequestered in the Golgi or ER. (A) Representative images of eGFP-tagged cells expressing FGFR WT, N550K and Y376C (green) fixed and stained for GM130 (magenta) to identify the Golgi, and DAPI (blue) as a nuclear stain. Insets indicate the close proximity of FGFR to Golgi structures (white arrowheads). Single channels from boxed regions in the merged image are displayed with inverted contrast. The Golgi is outlined in control cells with a dotted magenta line. The Golgi is fragmented in mutant-expressing cells. Scale bar: 20 µm. (B) Live-cell spinning disc confocal microscopy of Ishikawa cells stably expressing eGFP-tagged FGFR2 WT, Y376C or N550K (green) with an mCherry-tagged ER marker (Sec61–mCh, magenta). The input intensity range of the FGFR2-Y376C–eGFP image is scaled to 50% for display purposes to prevent saturation of vesicular structures. Vesicular structures are adjacent to ER in both wild-type and mutant-expressing cells and move unhindered in all conditions. Scale bar: 10 µm. (C) eGFP-tagged FGFR WT and Y376C receptor and ER dynamics at the cell periphery in the regions indicated by the boxes in B. Scale bar: 1 µm; time is in seconds, yellow dotted line marks cell periphery. (D) Live-cell spinning disc confocal microscopy of Ishikawa cells stably expressing eGFP-tagged FGFR2 WT or N550K (green) with an mCherry-tagged Golgi resident protein (mCh–Rab6, magenta). (E) Time-lapse sequence of dynamic behaviour of eGFP-tagged FGFR WT or N550K (green) and Rab6 Golgi dynamics (magenta) from boxed regions in D. White arrowheads in C and E correlate with eGFP vesicles in the time-lapse sequence. Time is in seconds.
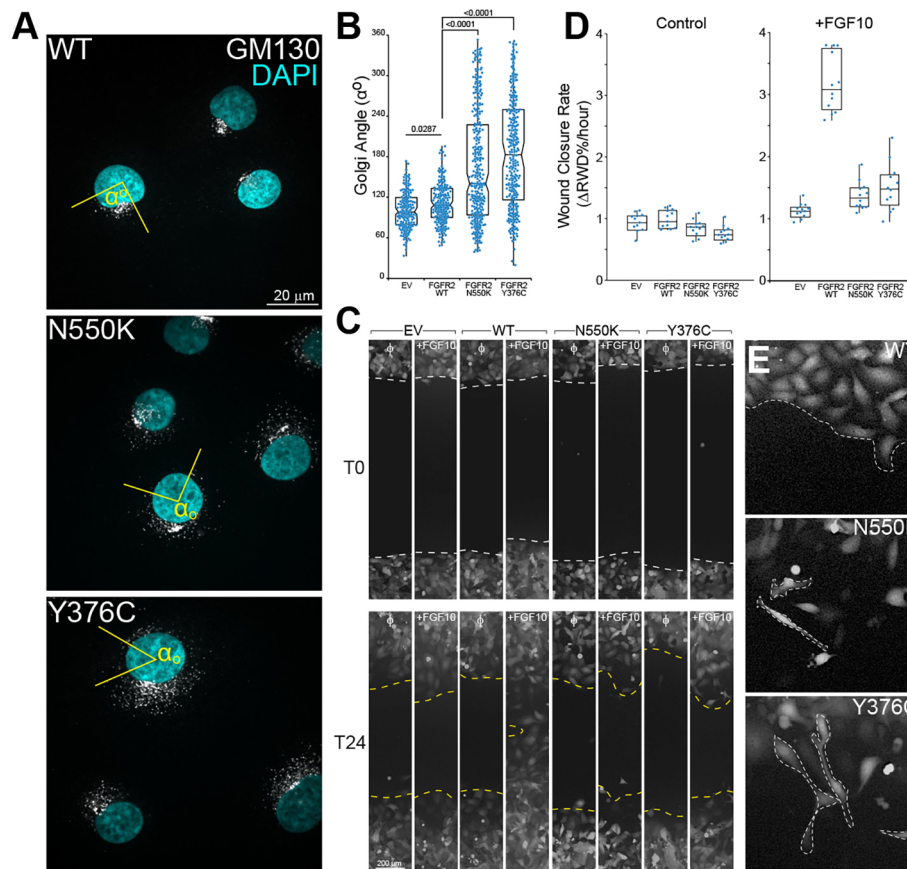
Fig. 4. A fragmented Golgi correlates with an aberrant migration phenotype in cells expressing mutant FGFR2. (A) Representative images of cells expressing eGFP-tagged FGFR2 WT, N550K and Y376C fixed and stained for the Golgi marker GM130 (white), and DAPI as a nuclear stain (cyan). (B) Quantification of the degree of Golgi fragmentation around the nucleus in sub-confluent Ishikawa cell monolayers. The Golgi fragmentation angle α (yellow line in A) was defined as the angle through the centre of the nucleus that encompasses all Golgi structures. n=149 (EV), 121 (WT), 227 (N550K), 189 (Y376C). Data are three biological repeats combined. Box-and-whisker plots show the median, first and third quartile (box), and 95% confidence intervals (notches), with whiskers extending to the furthest observations within ±1.5 times the interquartile range. Dots are individual data points. P-values were calculated with a non-parametric Kruskal–Wallis analysis of variance with Bonferroni error correction, and are displayed on graph. (C) Scratch wound healing assay in Ishikawa cells stably overexpressing FGFR2 WT, N550K and Y376C with co-transduced mCherry to allow for high contrast imaging and tracking. Cells were pre-treated with 10 μg/ml Mitomycin C for 1 h, wounded and serum starved (0.5% FBS) for 2 h. Cells were stimulated with heparin (5 μg/ml; control) or FGF10 (50 μg/ml) in the presence of heparin, in medium with 2% serum. Dashed lines represent the edge of the wound. (D) Analysis of cell migration rates (relative wound density/time) in control or with FGF10. Relative wound density was calculated by IncuCyte™ Chemotaxis Cell Migration Software. Frames were acquired every 2 h for a 24 h period. The wound closure rate was calculated by measuring the slope of the line between t0 and the final time at 24 h. Dots are individual data points. Each box-and-whisker plot represents the median, first and third quartiles (boxes) and 95% confidence intervals (notches) with whiskers extending to the furthest observations within ±1.5 times the interquartile range (IQR), of three independent experiments with n=4 biological replicates per condition/experiment. (E) Representative frames from time-lapse data demonstrating aberrant cell morphology phenotype of mutant cells at wound edges. Outlines of cells are highlighted with a dotted line.

surface (Fig. 6A–C, upper panels). In 3D acini, WT FGFR2 displayed a predominant plasma membrane localization as well as localization to intracellular puncta (Fig. S5). Similar to what was observed in 2D, in 3D this intracellular localization was enhanced in FGFR2 mutants. In contrast to WT acini, and similar to our single-cell findings, Golgi orientation and polarity was lost in FGFR2 mutant acini as evidenced by the failure of β4-integrin to localize to the basal surface (Fig. 6A–C, lower panels corresponding to N550K and Y376C acini). Moreover, we observed differences in morphology in the acini from cells expressing each of the mutants. Acini formed from N550K cells exhibited a multi-lobular phenotype, a structure that consisted of multiple lobules of smaller acini that we revealed to be connected by creating complete maximum intensity projections of F-actin z-sections (Fig. 6A, red and blue dotted outlines). In contrast, Y376C acini grew as larger, amorphous bulging structures, appearing to be double the size of control WT acini. This observation was supported by analysis of

acini size (8 day, Fig. 6D; mean size: empty vector 3343 μm^2, WT 3447 μm^2, N550K 5901 μm^2, Y376C 9217 μm^2), indicating that in a 3D environment, the expression of the activating FGFR mutants increases proliferation in comparison to WT. As we observe a perturbed Golgi in both mutants, these results suggest that, although individual mutations can result in different modulation of downstream molecules, these appear to converge on the common target of Golgi orientation and polarity.

To test whether the activating mutants had an effect on migration in a collective context, we generated acini (day 3) and examined their multicellular dynamics using time-lapse differential interference contrast microscopy in the presence and absence of FGF10 for 72 h. To understand the variation of migration and invasion phenotypes that we observed during time-lapse imaging, acini morphology was classified into three categories: spherical, lobular/branching and protrusive/bulging (see key in Fig. 6F). The morphology of empty vector, WT, Y376C and N550K acini, was then scored in the
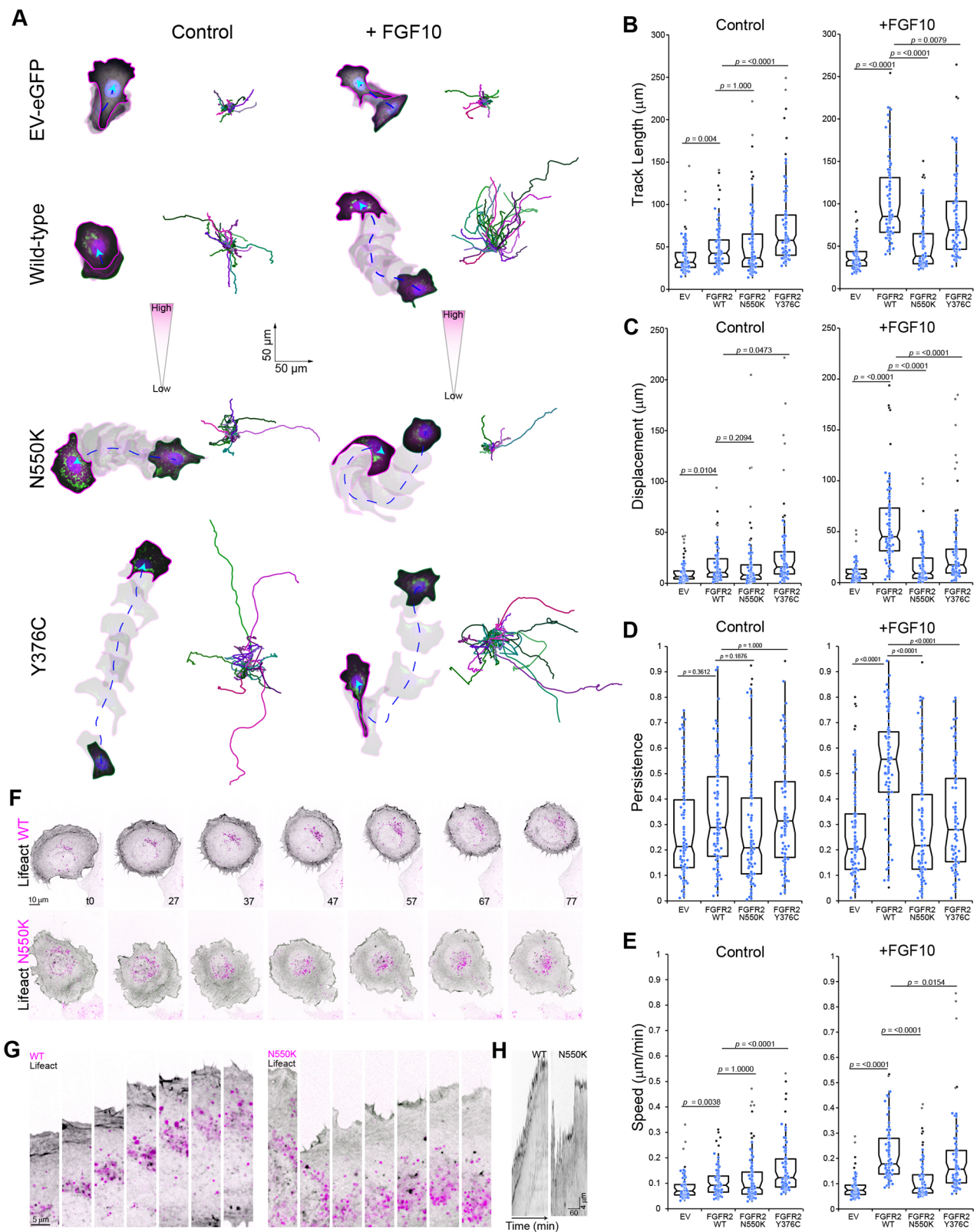
Fig. 5. See next page for legend.

presence and absence of FGF10 (Fig. 6E). Stimulation with FGF10 resulted in a mild increase in invasive-like protrusions at the matrix-abutting surface of acini comprising cells expressing WT receptor (Movie 7), which was not observed in empty vector controls. In

mutant-expressing acini, FGF10 stimulation resulted in increased invasion into the matrix. Cells expressing N550K preferentially exhibited more lobular/branching morphology with a slight increase upon the addition of ligand. This morphology correlated with a

Fig. 5. FGFR mutant cells do not migrate persistently during FGF-induced chemotaxis. (A) Spinning disc confocal time-lapse sequence of cells co-expressing mCherry (magenta) with EV-eGFP, eGFP-tagged FGFR WT or mutant (N550K, Y376C) (green), stimulated with a chemotactic gradient (low–high) of heparin alone (5 µg/ml, control) or heparin plus FGF10 (50 ng/ml), in medium with 2% serum. Hoechst 33342 was used to identify cell nuclei (blue). Cell outlines displayed are traces outlined every 50 min for 8 h. The initial frame (t0) is outlined in green and the final frame is outlined in magenta; remaining time points are opaque. Cell migration paths are outlined in blue (dotted line). Plots of representative cell migration paths in control (heparin) and FGF-treated cells (50 ng/ml). The 30 longest paths from each condition are displayed. Cells were tracked in Imaris (Bitplane) using the 'ImarisTrack' function using the analysis criteria outlined in the Materials and Methods. Migration paths were normalized to the starting position. Representative data set of three independent experiments. Analysis of cell migration from three experiments, n=90 cells per condition. (B) Total track length (µm), (C) cell displacement (shortest distance between t0 and the final frame; µm), (D) persistence index (ratio of cell displacement to total track length) and (E) cell migration speed (µm/min). The box-and-whisker plots show median, first and third quartiles (boxes) and 95% confidence intervals (notches) with whiskers extending to the furthest observations within ±1.5 times the interquartile range (IQR). Dots are individual data points. Black dots are outliers >1.5 and <3 the IQR, grey dots are outliers >3 IQR. P-values were calculated with a non-parametric Kruskal–Wallis analysis of variance with Bonferroni error correction. (F) Spinning disc confocal microscopy of Ishikawa cells co-expressing either a wild-type (WT) or activing mutant (N550K) FGFR2-eGFP (magenta) with mCherry–Lifeact (black), stimulated with FGF10 (50 ng/ml). Time is in min. (G) Higher magnification regions of the advancing cell edge of cells in F. (H) Kymograph of actin dynamics in WT and N550K expressing cells. Time scale is in min.

greater propensity for cells to leave the acini and migrate into the matrix, both in chains and as individual cells. In contrast, Y376C-expressing cells tended to undergo a bulging and protrusive type of growth, bubbling and pushing into the matrix, with an increase in lobular/branching invasive migration upon the addition of ligand. These findings suggest that the increased proliferation, and loss of multicellular polarity in combination with an increased propensity to invade, observed with activating FGFR mutations may play an important role in the pathology of FGFR-associated endometrial cancer.

DISCUSSION

Growth factor-driven cell migration is significantly linked to the dissemination of tumour cells, a process in carcinomas that typically requires invasion of cells as a cohesive group termed 'collective invasion' (Friedl et al., 2012). Although the spotlight for growth-factor driven invasion has long been focused on EGFR, relatively little is known about the role of FGFR, despite the evaluation of multiple anti-FGFR agents in ongoing phase I and II clinical trials (Babina and Turner, 2017). The majority of research pertaining to FGFR-dependent migration has focused on its role in development and wound healing, where it plays a role in collective migration (Vitorino and Meyer, 2008). This study examined the molecular mechanisms underpinning why patients diagnosed with endometrial cancer are at a greater risk of metastasis if they carry FGFR2-activating mutations. To accomplish this goal, we used a well-differentiated cell model of endometrial cancer to study the molecular mechanisms of two common endometrial cancer FGFR2-activating mutations, N550K and Y376C. To our knowledge, our study is the first to connect cancer-associated point mutations in FGFR2 to the loss of collective cell polarity, resulting in cancer cell invasion.

RTKs classically localize to and signal from the cell surface; however, signalling from intracellular membranes is now a rapidly

developing paradigm of cell biology (Murphy et al., 2009). The importance of compartmentalization of signalling has been exemplified by Ras and c-Met, whereby signalling from different subcellular organelle membranes has shown to exhibit altered temporal signalling dynamics and have different functional outcomes (Chiu et al., 2002; Aran and Prior, 2013). Although our studies do not preclude that FGFR2 mutants may go to an as-yet-unidentified extra endosomal compartment, they do indicate that they are signalling from an intracellular location. Interestingly, the extracellular allosteric FGFR inhibitor (SSR128129E) demonstrates 'biased antagonism' whereby the inhibitor can block downstream MAPK signalling but not PLCγ phosphorylation, supporting the concept that these pathways can be activated from different subcellular compartments (Herbert et al., 2016). Future studies will be directed towards understanding the role that mutant receptor spatio-temporal localization may play in perturbing Golgi structure, cell polarity and differential signalling.

Our detailed functional assays demonstrate that, in 2D, both activating mutations result in a perturbation of Golgi integrity and a loss of directional migration despite having different levels of receptor activation evident from western blotting. In basal conditions (10% FBS), N550K shows a significant increase in receptor phosphorylation in addition to higher FRS2α and PLCγ activation than Y376C and WT, yet greater migration is observed for Y376C. Despite these differences, both mutations show a loss of directional migration in response to FGF10. Similarly, in the 2D proliferation assays, N550K showed less proliferation than Y376C despite higher constitutive receptor phosphorylation. Analysis of FRS2α and PLCγ phosphorylation over time following stimulation with FGF10 (Fig. 2) showed a greater persistence of signalling downstream for Y376C compared to N550K, suggesting that the enhanced phenotypic effects seen with Y376C could be the result of changes in temporal signalling downstream of these mutations. This is further supported by our finding that Y376C exhibits a decrease in FGF10-mediated receptor internalization dynamics in comparison to N550K and WT. Our 3D proliferation assays demonstrate that both mutations lead to increased proliferation as evidenced by increased acini size but result in strikingly different acini morphologies, suggesting that the differences we observe in signalling may be enhanced in an environment that better recapitulates the epithelial structure of the endometrium. This is supported by our observed differences in their modes of invasion into the matrix, where a more branching invasive phenotype was observed in the N550K acini, compared to the bulging or pushing into the matrix we more frequently observe in Y376C acini. These data suggest that although both FGFR2 mutations increase proliferation and invasion in endometrial cancer cells, there are significant differences in adaptor and effector signalling molecules utilized by these two different activating mutations. These differences will be investigated in the future with detailed phospho-proteomics.

This study highlights the importance of performing functional assays using 3D models to better understand cancer-associated mutations. These studies revealed a loss of apico-basal polarity in both activating mutants, an important step during the progression of cancer (Muthuswamy and Xue, 2012) and one associated with increased metastatic capacity. Interestingly, Ishikawa cells form lumen-containing, polarized acini, even though they lack expression of the key apico-basal polarity proteins Par3 and PTEN (Weigelt et al., 2013; Williams et al., 2017). Despite both mutants causing a loss of apico-basal polarity and an absence of basement membrane, N550K-expressing cells tended to be more invasive while Y376C-expressing cells instead preferentially proliferated, pushing against
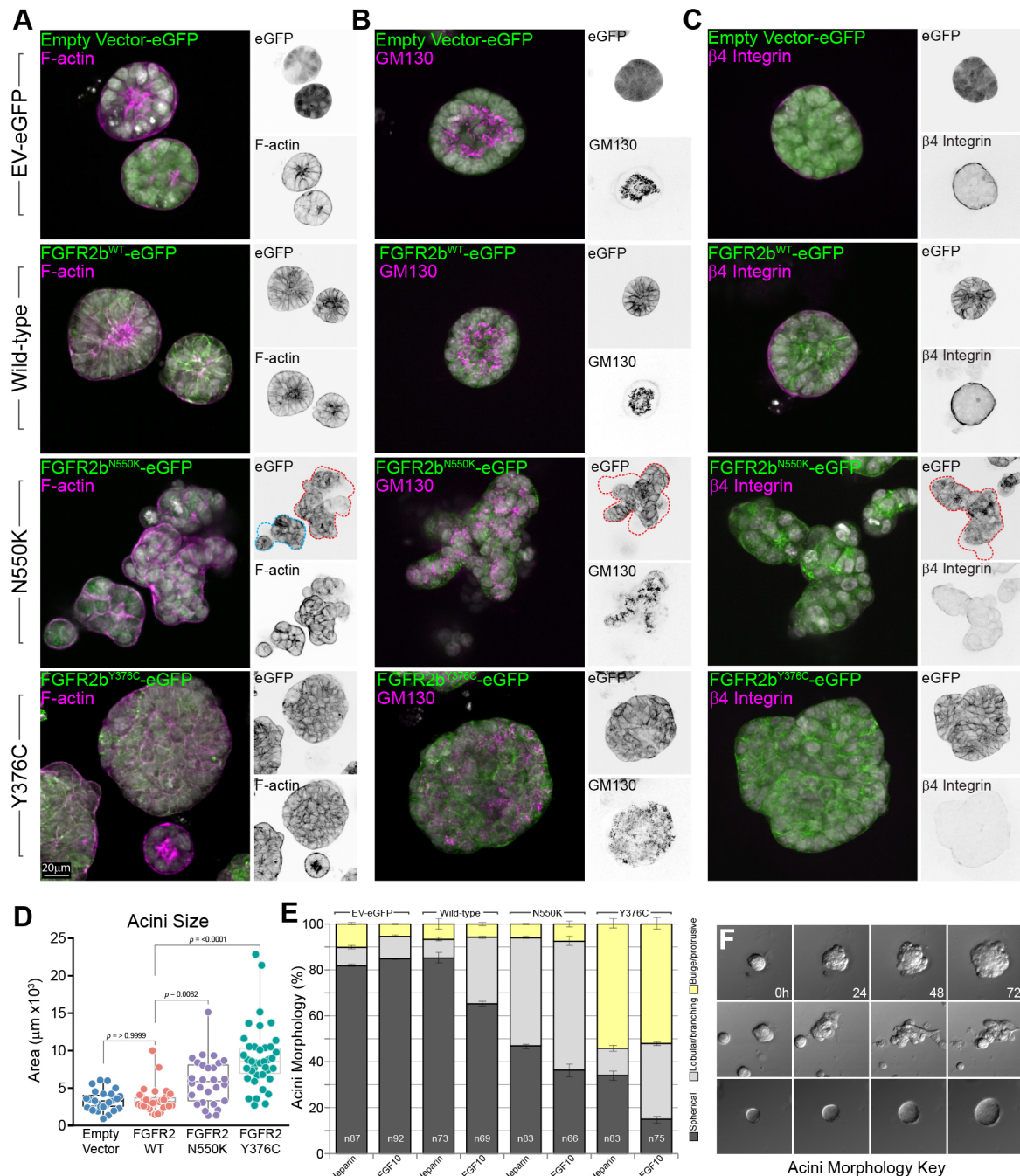
Fig. 6. Effects of FGFR activating mutations on endometrial acinar morphogenesis. (A) Maximum intensity projections of four, 2 µm spinning disc confocal optical sections of Ishikawa acini grown in growth factor-reduced Matrigel™ overlay assay. Ishikawa cells expressing empty vector (EV-eGFP), eGFP-tagged (green) wild-type, or mutant N550K or Y376C FGFR grown for 8 days to form acini. Acini are co-stained for DAPI (white) and for F-actin (phalloidin) (A), the Golgi (GM130) (B) or the basement membrane (β4 integrin; magenta) (C). Blue and red dashed line indicate the outline of the complete maximum intensity volume reconstruction. (D) Quantification of 8-day acinus size. Box-and-whisker plots show median, first and third quartile (box), and 95% confidence intervals (notches) with whiskers extending to the furthest observations within ±1.5 times the interquartile range. Dots are individual data points. *P*-values were calculated by non-parametric Kruskal–Wallis analysis of variance with Dunn's multiple comparisons test correction and are displayed on graph. (E) Quantification of acinus morphology phenotypes observed from time-lapse imaging (72 h) of cells expressing empty vector (EV-eGFP), eGFP-tagged wild-type or mutant (N550K, Y376C) FGFR, stimulated with either heparin alone or heparin plus FGF10 in 2% serum. Acinus phenotypes were categorized as spherical, bulging/lobular or protrusive/bulging. All three phenotypes were observed in each condition at different ratios. Analysis (mean±s.e.m.) is from three combined experiments; *n* values are displayed on graph. (F) Acini morphology key corresponding to graph E. See Movie 7.

the ECM, although switching to an invasive phenotype upon the addition of ligand.

The loss of multicellular polarity and resulting invasive phenotype we observe in our FGFR-activating mutants can be linked to our novel observation connecting FGFR2 mutant expression to a perturbation of Golgi morphology. Orientation of the Golgi towards the leading edge of a migrating cell is thought to elicit efficient delivery of membrane components and signalling

required for motility. In addition to a loss of Golgi polarization, we observed that mutant cells failed to reorient their intracellular FGFR pool towards the leading edge, which correlated with a lack of productive migration. Interestingly, FGF signalling has recently been linked to Golgi orientation during craniofacial development (Li et al., 2013). Ectopic activation of FGFR2 signalling in cranial neural crest cells with FGF8 or FGFR2^{C278F} and detailed quantification of the Golgi angles 72 h later, showed a more randomized Golgi distribution indicative of altered cell polarity compared to normal embryos. In further support of our findings, activation of inducible FGFR1 and FGFR2 with the dimerizing agents AP20187 has been shown to lead to a loss of apico-basal polarity in a model of primary mammary epithelial cell 3D culture (Xian et al., 2007), although changes to the Golgi were not examined in this model.

From a clinical perspective, endometrial cancer patients with early disease (stage I/II) that carry somatic activating FGFR2 mutations show an increased risk of disease recurrence (Byron et al., 2012; Jeske et al., 2017). Decreased cancer-specific survival is also seen in endometrial cancer patients with somatic FGFR2 mutations, irrespective of stage (Jeske et al., 2017). We propose that the loss of multicellular polarity and increased invasion we have observed in Ishikawa cells carrying two common hotspot mutations in FGFR2 results in an increase in metastasis from the primary site, likely increasing the risk for recurrent disease despite surgical resection of the primary tumour. This study performed within an appropriate endometrial cancer context also has additional translational implications. Specifically, the increased localization of mutant receptors to a perinuclear pool suggests that therapeutic agents targeting cell surface receptors such as neutralizing antibodies (Bai et al., 2010) or the novel extracellular allosteric inhibitors SSR128129E or Alofanib (Herbert et al., 2016; Tsimafeyeu et al., 2016) will not be as effective as small molecule kinase inhibitors that can block signalling independent of receptor localization.

MATERIALS AND METHODS
Cell culture
HEK-293FT (Invitrogen) cells were cultured in DMEM (Gibco), 10% fetal bovine serum (FBS, Gibco), 100 µg/ml penicillin, 100 µg/ml streptomycin and 0.1 mM MEM non-essential amino acids. HEK-293FT cells were supplemented with 2 mM L-glutamine and 0.5 mg/ml Geneticin/G418 (Invitrogen, 10131035). pLex307-transduced Ishikawa cells were maintained in 2.5 µg/ml puromycin dihydrochloride (Invitrogen, A11138-03), whereas pLenti6-transduced cells were maintained in 5 µg/ml Blasticidin (Invitrogen, 461120). Cell lines were authenticated by STR profiling (QIMR Berghofer Medical Research Institute).

DNA constructs and lentiviral vectors
FGFR2^{WT}–eGFP and mutant FGFR2^{N550K}–eGFP and ^{Y376C}–eGFP were made by sub-cloning the epithelial b isoform of FGFR2 (a gift from Zamal Ahmed and John E. Ladbury, M.D. Anderson Cancer Center, Houston, TX) in frame with the eGFP tag, including a seven amino acid linker region, in the entry vector pENTR1A-GFP-N2 (Addgene plasmid #19364, deposited by Eric Campeau; Campeau et al., 2009), then recombined into pLex307 (Addgene plasmid #41392 deposited by David Root, MIT, Cambridge, MA), using LR clonase (Invitrogen 11791-100) with slight modifications to the manufacturer's instructions as previously described (Stehbens et al., 2012). pLenti-LifeAct mCherry was a generous gift from Diane Barber (UCSF, San Francisco, CA), pLenti6 pmRab6-mCherry, pLenti6 pmCherry-Sec61 Lentiviral particles were produced in HEK293FT cells using packaging plasmids as previously described (Byron et al., 2013; Stehbens et al., 2012, 2014). To generate stable fluorescent protein-expressing Ishikawa cell lines, cells were seeded to be 70% confluent on the

day of infection in a 60 mm dish. Cells were incubated with lentiviral particles for 16 h with 5 µg/ml polybrene (Millipore TR-1003) before selection in 2.5 µg/ml puromycin for 2 weeks. Homogenous low expression levels were selected for by performing FACS and analysed by live-cell imaging and western blot analysis of eGFP. For scratch wound and migration assays, cells expressing eGFP-tagged WT, N550K or Y376C FGFR, or eGFP vector alone, were infected with empty vector pLex307 mCherry and selected for by fluorescence-activated cell sorting to enable high-contrast visualization and quantification.

Antibodies, immunofluorescence and immunoblotting
Primary antibodies used for immunofluorescence and immunoblotting, including specific dilutions, are listed in Table S1. All secondary fluorescently labelled antibodies were highly cross-absorbed secondary antibodies from Jackson ImmunoResearch. For 2D immunofluorescence, samples were fixed with 4% paraformaldehyde (PFA; EM grade, 15710, Electron Microscopy Services) in BRB80 buffer (80 mM K-PIPES, pH 6.8, 1 mM MgCl$_2$, 1 mM EGTA) for 20 min at room temperature, washed three times with PBS and permeabilized with 0.25% Triton X-100 in PBS for 5 min. Samples were rinsed three to five times in blocking buffer (2% BSA, 0.1% Triton X-100, 0.1% NaN$_3$ in PBS). Samples were incubated with primary antibodies diluted in blocking buffer for 1 h at room temperature. Samples were rinsed three to five times in blocking buffer for 5–10 min each before incubating in secondary antibodies (1:500) for 45 min at room temperature. Secondary antibodies and phalloidin were diluted in blocking buffer. Samples were rinsed three to five times in PBS, for 5–10 min each, then mounted in Mowiol mounting medium {0.1 M Tris-HCl pH 8.5, 25% glycerol, 10% Mowiol 4-88; 475904, Calbiochem, 2% DABCO [1,4-Diazabicyclo(2.2.2)octane, D2522, Sigma]}. For 3D assays immunofluorescence was analysed as described previously (O'Brien et al., 2006). In brief, samples were washed two times quickly with PBS+ (PBS supplemented with 0.9 mM CaCl$_2$ and 0.5 mM MgCl$_2$) at room temperature before fixation with 4% PFA diluted in BRB80 for 20 min at room temperature. Samples were washed twice with PBS+ for 5–10 min each before permeabilizing with 0.5% Triton X-100, PBS for 10 min at 4°C, then placed in PFS blocking solution (PBS+, 0.7% fish skin gelatin, 10% saponin, 0.02% NaN$_3$) for 30–60 min at room temperature, with gentle shaking. Primary antibodies were diluted in PFS and incubated for 2 h at room temperature with gentle rocking. Samples were then washed three times for 5 min each in PFS with gentle rocking at room temperature. Samples were incubated with secondary antibody diluted in PFS for 60 min at room temperature with gentle rocking before washing three times for 5 min each in PFS. Samples were stored at 4°C in PBS+, 0.02% NaN$_3$ and 0.1% n-propyl gallate anti-fade.

For immunoblotting, cells were washed once with ice-cold PBS before lysis in ice-cold RIPA buffer (50 mM Tris-HCl, pH 7.5, 150 mM NaCl, 1 mM EDTA, 1 mM EGTA, 1% Triton X-100, 1% sodium deoxycholate, 0.1% sodium dodecyl sulfate and protease inhibitors) containing phosphatase inhibitors (50 mM NaF, 1 mM NaVO$_4$ and 10 mM sodium pyrophosphate) for 5 min on ice, scraped off the tissue culture dish, transferred to an Eppendorf tube, and incubated on ice for an additional 5 min. Cell lysates were sonicated at 50% amplitude, three times at 2 s intervals, with 30 s rest on ice between intervals. Cell lysates were then centrifuged at 21,130 g for 15 min and supernatants transferred to new tubes for either a BCA assay or to one containing SDS-PAGE sample buffer. Samples were heated to 100°C for 5 min, and centrifuged prior to loading. 20 µg of protein was loaded per lane onto a 5–15% gradient Tris-glycine gel. Proteins were separated by SDS-PAGE. Proteins were transferred by wet transfer for 2 h at 110 V onto nitrocellulose (Bio-Rad Mini Trans Blot Apparatus). Membranes were incubated for 1 h in blocking buffer (5% non-fat dry milk, TBS and 0.1% Tween-20) at 4°C. Primary antibodies were diluted (see Table S1 for dilutions) in 3% BSA blocking buffer and incubated with membrane for 2 h at room temperature on an orbital shaker, then washed five times in TBS with 0.1% Tween-20. Secondary horseradish peroxidase (HRP) conjugated antibodies were diluted 1:10,000 in 5% BSA-containing blocking buffer and incubated with membranes at room temperature for 1 h, washed ten times in TBS with 0.1% Tween-20, and rinsed once in TBS prior to incubation with ECL (WBLUF0100, Merck

Millipore). Membranes were imaged using a Quantum ST4 documentation system (Vilber Lourmat), cropped in Adobe Photoshop CS6 and assembled in Adobe Illustrator CS6. LUTs were adjusted linearly to enable comparison of protein of interest to loading controls.

Microscopy, image processing and data analysis

Scratch wound assays were imaged on an IncuCyte® ZOOM Live-Cell Analysis System (ESSEN BioScience). Live-cell digital interference contrast imaging was performed on an environmentally controlled Olympus CellR inverted IX83 microscope, equipped with a Hamamatsu Orca Flash 2.8 CCD camera, controlled by Olympus Xcellence software. Epifluorescence images were acquired on an Olympus BX63 epifluorescence microscope controlled using the CellSense Dimension 1.11 software (Olympus). SDC live-cell imaging was performed on an environmentally controlled Nikon Ti inverted microscope with a Borealis-modified Yokogawa CSU-X1 confocal head (Spectral Applied Research) and equipped with a Clara cooled scientific grade interline charge-coupled device (CCD) camera (Andor). Intracellular fluorescent protein-tagged protein dynamics were imaged at 37°C using either a ×60 or ×100 1.49 numerical aperture CFI apochromat TIRF objective (Nikon). TIRF images were acquired on the same TI inverted microscope stand (Nikon) equipped with a motorized TIRF illuminator (Nikon), an Evolve Delta electron-multiplying CCD camera (Photometrics) and a ×100 1.49 numerical aperture CFI Apochromat TIRF objective (Nikon) using ×1.5 intermediate magnification. Emission wavelengths were separated using a filter wheel (Sutter) mounted between microscope and electron-multiplying CCD camera. The details of this system are published elsewhere (Li et al., 2013). SDC microscope hardware was controlled by NIS Elements software (Nikon), and image processing and analysis was performed in NIS Elements. Generally, for display purposes, image contrast was linearly adjusted on the 14- or 16-bit raw data, images were low-pass filtered in NIS Elements (Detail level: 2), and processed with an unsharp mask filter (Power: 0.5; Area: 7). Figures were assembled using Adobe Photoshop and Illustrator CS5 (Adobe). Videos were assembled in Quicktime Pro (Apple). For live-cell microscopy, the growth medium was supplemented with 20 mM HEPES pH 7.5 (Gibco, 15630-080), and the glass-bottom dishes (Cellvis 4-Chamber 35 mm glass bottom dish with 20 mm microwell, #1.5 cover glass, D35C4-20-1.5-N) or eight-well chambers (IBIDI 8-well glass bottom: #1.5 cover glass, 80827) were sealed with vacuum grease to prevent medium evaporation. Eight-well chamber slides were fitted with a glass lid for DIC imaging (IBIDI DIC Lid for µ-Slides, 80055). Black/magenta image overlays were generated as described previously (Stehbens et al., 2014).

Ligand internalization assays

Cells expressing wild-type or mutant eGFP-tagged FGFR2b were plated onto glass-bottom dishes (Cellvis 4-Chamber 35 mm Glass Bottom Dish with 20 mm microwell, #1.5 cover glass, D35C4-20-1.5-N) to achieve 30% confluence the following day. Samples were rinsed three times in DMEM containing 0.5% FBS then starved at 37°C for 2 h. Starved cells were imaged prior to being stimulated with FGF10 (50 ng/ml) and heparin (5 µg/ml) in 2% FBS for 60 min. Frames were acquired every 3 min.

Cell proliferation assays

Sulforhodamine B (SRB) cell proliferation was performed as previously published (Vichai and Kirtikara, 2006), with the following modifications. Cells were seeded at 2500 cells per well in a 96-well plate, and cellular proliferation assessed over 4 days in medium containing 0.5% FBS and 5 µg/ml heparin, in the absence and presence of 50 ng/ml FGF-10. 100% methanol was used to fix cells, and absorbance was read at 564 nm (Multiskan Go, Thermo Fisher Scientific). All absorbance values were corrected to a medium-only well and normalized to the values at day 0.

Scratch wound assay

Cell scratch migration assays were carried out on the InCucyte Zoom (Essen BioScience) machine. Briefly, cells were seeded into image lock plates (Essen Bioscience) and wounded using the wound maker (Essen Bioscience), then starved in 0.5% FBS medium for 2 h before stimulation with 50 ng/ml FGF10 (R&D Systems FGF10 345-FG or Ray Biotech 213-10087-2AF) and 5 µg/ml heparin (Sigma-Aldrich, 3149) in 2% FBS-

supplemented medium. In all scratch wound migration assays, cells were treated with 10 µg/ml Mitomycin C (Sigma, M4287) for 1 h to inhibit proliferation. Wound closure was captured every 2 h for 24 h and analysed using IncuCyte Zoom software (Essen Bioscience). Relative wound density (RWD) was plotted against time. The rate of wound closure was calculated as the slope of this curve.

Chemokinesis migration assay

Chemokinesis migration assays were carried out on a custom-designed environmentally controlled SDC microscope as described previously (Turner and Grose, 2010). Cells were seeded onto glass bottom chamber slides and starved for 2 h in 0.5% FBS medium before stimulating with 50 ng/ml FGF10 and 5 µg/ml heparin in medium containing 2% FBS. Movies spanned 8 h, with frames captured every 5 min. Cell tracking was completed using Imaris software (Bitplane).

Chemotaxis migration assay

Random migration assays were carried out on a custom-designed environmentally controlled SDC microscope as described previously (Stehbens et al., 2012). To assess directional migration at a single-cell level, 10,000 cells were seeded onto one side of glass bottom chamber slides (IBIDI, 80827). Cells were allowed to adhere overnight while growing at an inclined angle of 45°. Cells were then washed twice with PBS and starved for 2 h in 0.5% FBS medium. 50 µl of growth factor-reduced Matrigel™ (GFR-MG; Corning, 354230, lot# 5313010) was then mixed with 50 ng/ml FGF-10 and 5 µg/ml heparin and allowed to solidify on the chamber wall opposite to adherent cells. Before imaging, medium was replaced with fresh 2% FBS-supplemented medium to allow the creation of a chemotactic gradient originating from the solidified Matrigel™.

Temporal signalling assay

Cells were grown to 50% confluence before being starved overnight in DMEM (Gibco, see above) containing 0.5% FBS. Following starvation, cells were stimulated with FGF10 (50 ng/ml) and heparin (5 µg/ml). At the indicated time intervals, cells were washed once in ice-cold PBS before lysates were collected in RIPA buffer containing protease inhibitors (see the Antibodies, immunofluorescence and immunoblotting section for details).

Cell surface biotinylation assay

Biotinylation experiments were performed as described previously (Adams et al., 2015). In brief, Ishikawa cells were either grown in 10% FBS medium or starved in 0.5% FBS medium for 2 h before being washed with PBS and biotinylated (Pierce, 21331) for 1 h at 4°C. Following biotinylation, cells were washed with PBS and lysed in RIPA buffer containing protease inhibitors (see above) and disrupted by sonication on ice. After removal of cellular debris by centrifugation (18,400 *g* for 10 min at 4°C), lysates were incubated with streptavidin beads (Cell Signaling Technology, 5947) overnight at 4°C.

3D acinus assays

Acini were formed as described previously (O'Brien et al., 2006). In brief, GFR-MG (Corning, 354230, lot# 5313010) was thawed on ice for 30 min. 20 µl of 100% GFR-MG was spread evenly across each well of a pre-chilled eight-well glass bottom chamber slide, placed on top of an inverted 10 cm dish over ice, using a chilled, flat p200 tip. The slide was then placed at 37°C and the GFR-MG allowed to set for 10–30 min while cell dilutions were prepared. A solution of 4% GFR-MG was prepared by diluting 100% GFR-MG with complete medium. The solution of detached cells was passed through a BD cell strainer (Corning, 352340), to ensure cells were fully separated and suspended, before being diluted to 20,000 cells/ml, then mixed 1:1 with the 4% GFR-MG solution. 300 µl of the cell–GFR-MG solution was added to each well of an eight-well chamber slide. The day of plating is considered day zero. Medium was changed 5 days after plating. For live-cell DIC time lapse imaging, day 3 acini were gently washed with 0.5% FBS three times, then serum starved for 120 min in 0.5% FBS. Acini were then stimulated with 50 ng/ml FGF10 (Ray Biotech, 213-10087-2AF) and 5 µg/ml heparin (Sigma-Aldrich, 3149) in 2% FBS-supplemented medium, or with heparin alone as a control. Acini were imaged for 72–96 h.

Acini morphology was classified as either, spherical, lobular/branching or protrusive/bulging, which were defined by growth characteristics observed over time and are displayed in Fig. 6F (morphology key). Spherical was defined as acini that were round, characteristic of polarized acini, lobular/branching were defined as acini where lobes would protrude from multiple sides of the acini, which would often result in branching of cells into the matrix and protrusive/bulging were defined as acini that appeared to push into the matrix with central bulging, consistent with non-polarized central divisions. Acini size (area) measurement was performed using NIS Elements AR 'area' tool of maximum intensity projection images from z-stacks of 8 day acini.

Vesicle size and dynamics
Vesicle size was measured using NIS Elements AR Version 5.01 (Nikon) using the General Analysis 3 Application. Two binary object masks were created by thresholding for object size and intensity to detect both small and large objects on images of live cells. Vesicle dynamics were measured using the 'binary tracking' tool on timelapse images. The mean square displacement of object tracks were calculated as a sum of squared distances from the beginning of the track.

Receptor surface localization analysis
TIRF images were acquired on live-cells plated on glass bottom dishes (Cellvis 4-Chamber 35 mm Glass Bottom Dish with 20 mm microwell, #1.5 cover glass, D35C4-20-1.5-N). $9 \times 6.5 \, \mu m^2$ regions of interest (ROIs) were placed within 1–10 μm along the free edge of the cells. All ROIs were background corrected (identical ROI in cell free area). Cell surface labelling was performed by performing immunofluorescence on eGFP–FGFR2b WT and mutant-expressing cells in non-permeabilized conditions (no detergents) using an N-terminal FGFR2 antibody. Cell outline ROIs were generated using the Bezier ROI tool in NIS elements. Background corrected, surface fluorescence intensity values (antibody fluorescence, 594 nm) were expressed as a ratio of total (eGFP fluorescence, 488 nm).

Golgi complex angle measurement
Golgi angle analysis were carried out using NIS-Elements AR Version 4.40 (Nikon) using the free angle measurement tool as described previously (Xian et al., 2007).

Scratch wound assay analysis
Scratch wound assay measurements are displayed as percentage (%) relative wound density (RWD). RWD was measured using InCucyte Zoom software and is a measurement of cell density of the wound area relative to cell density outside of the wound area over time. The RWD measurement is normalized for changes in cell density caused by proliferation and/or pharmacological treatment effects.

Cell migration analysis
For quantification, track lengths greater than 50% of the movie duration were selectively chosen while tracks 20 μm from the border were eliminated to exclude tracks that deviated out of frame. Random migration was defined by measuring the total change in distance (μm) and direction from the centre of each cell. Spider plots were created by mapping individual cell tracks and normalizing each point to 0,0 (x,y) to determine relative positions using:

$$Relative \; x \; or \; y \; position \; (\mu m) = x \; or \; y \; position^{Time \; Initial}$$
$$- x \; or \; y \; position^{Time \; current}.$$

Total path length (t) was calculated through:

$$\sum_{i=x,y \; Initial}^{x,y \; Final} \sqrt{(x^2) + (y^2)}.$$

Total displacement (d) was calculated using:

$$Displacement(d) = \sqrt{(x^2) + (y^2)}.$$

Persistence (m) was calculated:

$$Persistence(p) = \frac{d}{t}.$$

Software and statistical analysis
Microsoft Excel was used to perform statistical tests, graphing and the generation of spider plots. For statistical tests, the plug-ins Analyse-IT in conjunction with Kutools for Microscoft Excel or and Prism 7 (Graphpad) were used. Data sets were tested for normality using a Shaprio–Wilk test. A non-parametric, Kruskal–Wallis one-way analysis of variance with a Bonferroni correction or Dunn's multiple comparisons test was chosen to assess significance between independent samples (see figure legends). A significance value of 0.05 was taken as a cut-off for significance. Statistical summary for all data can be found in Table S2. Adobe Illustrator and Photoshop Creative Cloud 2015 were used to generate figures in this paper.

Author contributions
Conceptualization: S.J.S., D.M.B., P.M.P.; Methodology: S.J.S., R.J.J., N.K.H., D.M.B., P.M.P.; Validation: S.J.S., R.J.J.; Formal analysis: S.J.S., R.J.J.; Investigation: S.J.S., R.J.J., M.N.A., S.R.P.; Resources: P.M.P., N.K.H.; Data curation: S.J.S., R.J.J.; Writing - original draft: S.J.S., R.J.J., D.M.B., P.M.P.; Writing - review & editing: S.J.S., R.J.J., M.N.A., N.K.H., D.M.B., P.M.P.; Visualization: S.J.S., R.J.J., N.K.H.; Supervision: S.J.S., N.K.H., D.M.B., P.M.P.; Project administration: S.J.S., P.M.P.; Funding acquisition: P.M.P.

Supplementary information
Supplementary information available online at
http://jcs.biologists.org/lookup/doi/10.1242/jcs.213678.supplemental

References
Adams, M. N., Harrington, B. S., He, Y., Davies, C. M., Wallace, S. J., Chetty, N. P., Crandon, A. J., Oliveira, N. B., Shannon, C. M., Coward, J. I. et al. (2015). EGF inhibits constitutive internalization and palmitoylation-dependent degradation of membrane-spanning procancer CDCP1 promoting its availability on the cell surface. *Oncogene* **34**, 1375-1383.

Adar, R., Monsonego-Ornan, E., David, P. and Yayon, A. (2002). Differential activation of cysteine-substitution mutants of fibroblast growth factor receptor 3 is determined by cysteine localization. *J. Bone Miner. Res.* **17**, 860-868.

Ahmed, Z., Schuller, A. C., Suhling, K., Tregidgo, C. and Ladbury, J. E. (2008). Extracellular point mutations in FGFR2 elicit unexpected changes in intracellular signalling. *Biochem. J.* **413**, 37-49.

Aran, V. and Prior, I. A. (2013). Compartmentalized Ras signaling differentially contributes to phenotypic outputs. *Cell. Signal.* **25**, 1748-1753.

Babina, I. S. and Turner, N. C. (2017). Advances and challenges in targeting FGFR signalling in cancer. *Nat. Rev. Cancer* **17**, 318-332.

Bai, A., Meetze, K., Vo, N. Y., Kollipara, S., Mazsa, E. K., Winston, W. M., Weiler, S., Poling, L. L., Chen, T., Ismail, N. S. et al. (2010). GP369, an FGFR2-IIIb-specific antibody, exhibits potent antitumor activity against human cancers driven by activated FGFR2 signaling. *Cancer Res.* **70**, 7630-7639.

Baird, A., Esch, F., Mormède, P., Ueno, N., Ling, N., Böhlen, P., Ying, S. Y., Wehrenberg, W. B. and Guillemin, R. (1986). Molecular characterization of fibroblast growth factor: distribution and biological activities in various tissues. *Recent Prog. Horm. Res.* **42**, 143-205.

Barrow-Mcgee, R. and Kermorgant, S. (2014). Met endosomal signalling: in the right place, at the right time. *Int. J. Biochem. Cell Biol.* **49**, 69-74.

Bhattacharyya, D., Hammond, A. T. and Glick, B. S. (2010). High-quality immunofluorescence of cultured cells. *Methods Mol. Biol.* **619**, 403-410.

Bryant, D. M. and Mostov, K. E. (2008). From cells to organs: building polarized tissue. *Nat. Rev. Mol. Cell Biol.* **9**, 887-901.

Byron, S. A., Gartside, M. G., Wellens, C. L., Mallon, M. A., Keenan, J. B., Powell, M. A., Goodfellow, P. J. and Pollock, P. M. (2008). Inhibition of activated fibroblast growth factor receptor 2 in endometrial cancer cells induces cell death despite PTEN abrogation. *Cancer Res.* **68**, 6902-6907.

Byron, S. A., Gartside, M. G., Wellens, C. L., Goodfellow, P. J., Birrer, M. J., Campbell, I. G. and Pollock, P. M. (2010). FGFR2 mutations are rare across histologic subtypes of ovarian cancer. *Gynecol. Oncol.* **117**, 125-129.

Byron, S. A., Gartside, M., Powell, M. A., Wellens, C. L., Gao, F., Mutch, D. G., Goodfellow, P. J. and Pollock, P. M. (2012). FGFR2 point mutations in 466 endometrioid endometrial tumors: relationship with MSI, KRAS, PIK3CA, CTNNB1 mutations and clinicopathological features. *PLoS ONE* **7**, e30801.

Byron, S. A., Chen, H., Wortmann, A., Loch, D., Gartside, M. G., Dehkhoda, F., Blais, S. P., Neubert, T. A., Mohammadi, M. and Pollock, P. M. (2013). The N550K/H mutations in FGFR2 confer differential resistance to PD173074, dovitinib, and ponatinib ATP-competitive inhibitors. *Neoplasia* **15**, 975-988.

Campeau E, Ruhl VE, Rodier F, Smith CL, Rahmberg BL, Fuss JO, Campisi J, Yaswen P, Cooper PK, Kaufman PD. (2009). A versatile viral system for expression and depletion of proteins in mammalian cells. PLoS ONE **4**, e6529.

Chen, H., Ma, J., Li, W., Eliseenkova, A. V., Xu, C., Neubert, T. A., Miller, W. T. and Mohammadi, M. (2007). A molecular brake in the kinase hinge region regulates the activity of receptor tyrosine kinases. *Mol. Cell* **27**, 717-730.

Chiu, V. K., Bivona, T., Hach, A., Sajous, J. B., Silletti, J., Wiener, H., Johnson, R. L., Cox, A. D. and Philips, M. R. (2002). Ras signalling on the endoplasmic reticulum and the Golgi. *Nat. Cell Biol.* **4**, 343-350.

Citores, L., Bai, L., Sørensen, V. and Olsnes, S. (2007). Fibroblast growth factor receptor-induced phosphorylation of STAT1 at the Golgi apparatus without translocation to the nucleus. *J. Cell. Physiol.* **212**, 148-156.

Creutzberg, C. L., van Putten, W. L. J., Koper, P. C. M., Lybeert, M. L. M., Jobsen, J. J., Wárlám-Rodenhuis, C. C., De Winter, K. A. J., Lutgens, L. C. H. W., Van Den Bergh, A. C. M., Van De Steen-Banasik, E. et al. (2000). Surgery and postoperative radiotherapy versus surgery alone for patients with stage-1 endometrial carcinoma: multicentre randomised trial. PORTEC study group. post operative radiation therapy in endometrial carcinoma. *Lancet* **355**, 1404-1411.

Debnath, J. and Brugge, J. S. (2005). Modelling glandular epithelial cancers in three-dimensional cultures. *Nat. Rev. Cancer* **5**, 675-688.

Dienstmann, R., Rodon, J., Prat, A., Perez-Garcia, J., Adamo, B., Felip, E., Cortes, J., Iafrate, A. J., Nuciforo, P. and Tabernero, J. (2014). Genomic aberrations in the FGFR pathway: opportunities for targeted therapies in solid tumors. *Ann. Oncol.* **25**, 552-563.

Etienne-Manneville, S. (2004). Cdc42–the centre of polarity. *J. Cell Sci.* **117**, 1291-1300.

Ferlay, J., Soerjomataram, I., Dikshit, R., Eser, S., Mathers, C., Rebelo, M., Parkin, D. M., Forman, D. and Bray, F. (2015). Cancer incidence and mortality worldwide: sources, methods and major patterns in GLOBOCAN 2012. *Int. J. Cancer* **136**, E359-E386.

Foldynova-Trantirkova, S., Wilcox, W. R. and Krejci, P. (2012). Sixteen years and counting: the current understanding of fibroblast growth factor receptor 3 (FGFR3) signaling in skeletal dysplasias. *Hum. Mutat.* **33**, 29-41.

Friedl, P., Locker, J., Sahai, E. and Segall, J. E. (2012). Classifying collective cancer cell invasion. *Nat. Cell Biol.* **14**, 777-783.

Halaoui, R., Rejon, C., Chatterjee, S. J., Szymborski, J., Meterissian, S., Muller, W. J., Omeroglu, A. and Mccaffrey, L. (2017). Progressive polarity loss and luminal collapse disrupt tissue organization in carcinoma. *Genes Dev.* **31**, 1573-1587.

Harada, D., Yamanaka, Y., Ueda, K., Nishimura, R., Morishima, T., Seino, Y. and Tanaka, H. (2007). Sustained phosphorylation of mutated FGFR3 is a crucial feature of genetic dwarfism and induces apoptosis in the ATDC5 chondrogenic cell line via PLCgamma-activated STAT1. *Bone* **41**, 273-281.

Hatch, N. E., Hudson, M., Seto, M. L., Cunningham, M. L. and Bothwell, M. (2006). Intracellular retention, degradation, and signaling of glycosylation-deficient FGFR2 and craniosynostosis syndrome-associated FGFR2C278F. *J. Biol. Chem.* **281**, 27292-27305.

Herbert, C., Schieborr, U., Saxena, K., Juraszek, J., De Smet, F., Alcouffe, C., Bianciotto, M., Saladino, G., Sibrac, D., Kudlinzki, D. et al. (2016). Molecular mechanism of SSR128129E, an extracellularly acting, small-molecule, allosteric inhibitor of FGF receptor signaling. *Cancer Cell* **30**, 176-178.

Jean, S., Mikryukov, A., Tremblay, M. G., Baril, J., Guillou, F., Bellenfant, S. and Moss, T. (2010). Extended-synaptotagmin-2 mediates FGF receptor endocytosis and ERK activation in vivo. *Dev. Cell* **19**, 426-439.

Jeske, Y. W., Ali, S., Byron, S. A., Gao, F., Mannel, R. S., Ghebre, R. G., Disilvestro, P. A., Lele, S. B., Pearl, M. L., Schmidt, A. P. et al. (2017). FGFR2 mutations are associated with poor outcomes in endometrioid endometrial cancer: an NRG oncology/gynecologic oncology group study. *Gynecol. Oncol.* **145**, 366-373.

Kupfer, A., Kronebusch, P. J., Rose, J. K. and Singer, S. J. (1987). A critical role for the polarization of membrane recycling in cell motility. *Cell Motil. Cytoskeleton* **8**, 182-189.

Lee, G. Y., Kenny, P. A., Lee, E. H. and Bissell, M. J. (2007). Three-dimensional culture models of normal and malignant breast epithelial cells. *Nat. Methods* **4**, 359-365.

Li, X., Young, N. M., Tropp, S., Hu, D., Xu, Y., HallgrãMsson, B. and Marcucio, R. S. (2013). Quantification of shape and cell polarity reveals a novel mechanism underlying malformations resulting from related FGF mutations during facial morphogenesis. *Hum. Mol. Genet.* **22**, 5160-5172.

Lievens, P.-M., Mutinelli, C., Baynes, D. and Liboi, E. (2004). The kinase activity of fibroblast growth factor receptor 3 with activation loop mutations affects receptor trafficking and signaling. *J. Biol. Chem.* **279**, 43254-43260.

Lievens, P. M.-J., Roncador, A. and Liboi, E. (2006). K644E/M FGFR3 mutants activate Erk1/2 from the endoplasmic reticulum through FRS2 alpha and PLC gamma-independent pathways. *J. Mol. Biol.* **357**, 783-792.

Lin, C.-C., Melo, F. A., Ghosh, R., Suen, K. M., Stagg, L. J., Kirkpatrick, J., Arold, S. T., Ahmed, Z. and Ladbury, J. E. (2012). Inhibition of basal FGF receptor signaling by dimeric Grb2. *Cell* **149**, 1514-1524.

Longoria, T. C. and Eskander, R. N. (2015). Immunotherapy in endometrial cancer - an evolving therapeutic paradigm. *Gynecol. Oncol. Res. Pract.* **2**, 11.

Mattheyses, A. L., Simon, S. M. and Rappoport, J. Z. (2010). Imaging with total internal reflection fluorescence microscopy for the cell biologist. *J. Cell Sci.* **123**, 3621-3628.

Melan, M. A. and Sluder, G. (1992). Redistribution and differential extraction of soluble proteins in permeabilized cultured cells. Implications for immunofluorescence microscopy. *J. Cell Sci.* **101**, 731-743.

Ménard, L., Parker, P. J. and Kermorgant, S. (2014). Receptor tyrosine kinase c-Met controls the cytoskeleton from different endosomes via different pathways. *Nat. Commun.* **5**, 3907.

Miller, P. M., Folkmann, A. W., Maia, A. R. R., Efimova, N., Efimov, A. and Kaverina, I. (2009). Golgi-derived CLASP-dependent microtubules control Golgi organization and polarized trafficking in motile cells. *Nat. Cell Biol.* **11**, 1069-1080.

Mohammadi, M., Honegger, A. M., Rotin, D., Fischer, R., Bellot, F., Li, W., Dionne, C. A., Jaye, M., Rubinstein, M. and Schlessinger, J. (1991). A tyrosine-phosphorylated carboxy-terminal peptide of the fibroblast growth factor receptor (Flg) is a binding site for the SH2 domain of phospholipase C-gamma 1. *Mol. Cell. Biol.* **11**, 5068-5078.

Mohammadi, M., Olsen, S. K. and Ibrahimi, O. A. (2005). Structural basis for fibroblast growth factor receptor activation. *Cytokine Growth Factor. Rev.* **16**, 107-137.

Murphy, J. E., Padilla, B. E., Hasdemir, B., Cottrell, G. S. and Bunnett, N. W. (2009). Endosomes: a legitimate platform for the signaling train. *Proc. Natl. Acad. Sci. USA* **106**, 17615-17622.

Muthuswamy, S. K. and Xue, B. (2012). Cell polarity as a regulator of cancer cell behavior plasticity. *Annu. Rev. Cell Dev. Biol.* **28**, 599-625.

O'Brien, L. E., Yu, W., Tang, K., Jou, T.-S., Zegers, M. M. P. and Mostov, K. E. (2006). Morphological and biochemical analysis of Rac1 in three-dimensional epithelial cell cultures. *Methods Enzymol.* **406**, 676-691.

Olsen, S. K., Ibrahimi, O. A., Raucci, A., Zhang, F., Eliseenkova, A. V., Yayon, A., Basilico, C., Linhardt, R. J., Schlessinger, J. and Mohammadi, M. (2004). Insights into the molecular basis for fibroblast growth factor receptor autoinhibition and ligand-binding promiscuity. *Proc. Natl. Acad. Sci. USA* **101**, 935-940.

Ornitz, D. M. and Itoh, N. (2001). Fibroblast growth factors. *Genome Biol.* **2**, REVIEWS3005.

Ornitz, D. M. and Itoh, N. (2015). The Fibroblast Growth Factor signaling pathway. *Wiley Interdiscip. Rev. Dev. Biol.* **4**, 215-266.

Pollock, P. M., Gartside, M. G., Dejeza, L. C., Powell, M. A., Mallon, M. A., Davies, H., Mohammadi, M., Futreal, P. A., Stratton, M. R., Trent, J. M. et al. (2007). Frequent activating FGFR2 mutations in endometrial carcinomas parallel germline mutations associated with craniosynostosis and skeletal dysplasia syndromes. *Oncogene* **26**, 7158-7162.

Riedl, J., Crevenna, A. H., Kessenbrock, K., Yu, J. H., Neukirchen, D., Bista, M., Bradke, F., Jenne, D., Holak, T. A., Werb, Z. et al. (2008). Lifeact: a versatile marker to visualize F-actin. *Nat. Methods* **5**, 605-607.

Robertson, S. C., Meyer, A. N., Hart, K. C., Galvin, B. D., Webster, M. K. and Donoghue, D. J. (1998). Activating mutations in the extracellular domain of the fibroblast growth factor receptor 2 function by disruption of the disulfide bond in the third immunoglobulin-like domain. *Proc. Natl. Acad. Sci. USA* **95**, 4567-4572.

Schnell, U., Dijk, F., Sjollema, K. A. and Giepmans, B. N. (2012). Immunolabeling artifacts and the need for live-cell imaging. *Nat. Methods* **9**, 152-158.

SGO Clinical Practice Endometrial Cancer Working Group, Burke, W. M., Orr, J., Leitao, M., Salom, E., Gehrig, P., Olawaiye, A. B., Brewer, M., Boruta, D., Herzog, T. J. and Shahin, F. A. (2014). Endometrial cancer: a review and current management strategies: part II. *Gynecol. Oncol.* **134**, 393-402.

Stehbens, S., Pemble, H., Murrow, L. and Wittmann, T. (2012). Imaging intracellular protein dynamics by spinning disk confocal microscopy. *Methods Enzymol.* **504**, 293-313.

Stehbens, S. J., Paszek, M., Pemble, H., Ettinger, A., Gierke, S. and Wittmann, T. (2014). CLASPs link focal-adhesion-associated microtubule capture to localized exocytosis and adhesion site turnover. *Nat. Cell Biol.* **16**, 558-570.

Taurin, S., Yang, C. H., Reyes, M., Cho, S., Coombs, D. M., Jarboe, E. A., Werner, T. L., Peterson, C. M. and Janát-Amsbury, M. M. (2018). Endometrial cancers harboring mutated fibroblast growth factor receptor 2 protein are successfully treated with a new small tyrosine kinase inhibitor in an orthotopic mouse model. *Int. J. Gynecol. Cancer* **28**, 152-160.

Temkin, S. M. and Fleming, G. (2009). Current treatment of metastatic endometrial cancer. *Cancer Control* **16**, 38-45.

Timsah, Z., Ahmed, Z., Lin, C.-C., Melo, F. A., Stagg, L. J., Leonard, P. G., Jeyabal, P., Berrout, J., O'neil, R. G., Bogdanov, M. et al. (2014). Competition between Grb2 and Plcgamma1 for FGFR2 regulates basal phospholipase activity and invasion. *Nat. Struct. Mol. Biol.* **21**, 180-188.

Tsimafeyeu, I., Daeyaert, F., Joos, J.-B., V. Aken, K., Ludes-Meyers, J., Byakhov, M. and Tjulandin, S. (2016). Molecular modeling, de novo design and synthesis of a novel, extracellular binding fibroblast growth factor receptor 2 inhibitor alofanib (RPT835). *Med. Chem.* **12**, 303-317.

Turner, N. and Grose, R. (2010). Fibroblast growth factor signalling: from development to cancer. *Nat. Rev. Cancer* **10**, 116-129.

Vichai, V. and Kirtikara, K. (2006). Sulforhodamine B colorimetric assay for cytotoxicity screening. *Nat. Protoc.* **1**, 1112-1116.

Villaseñor, R., Kalaidzidis, Y. and Zerial, M. (2016). Signal processing by the endosomal system. *Curr. Opin. Cell Biol.* **39**, 53-60.

Vitorino, P. and Meyer, T. (2008). Modular control of endothelial sheet migration. *Genes Dev.* **22**, 3268-3281.

Weigelt, B., Warne, P. H., Lambros, M. B., Reis-Filho, J. S. and Downward, J. (2013). PI3K pathway dependencies in endometrioid endometrial cancer cell lines. *Clin. Cancer Res.* **19**, 3533-3544.

Williams, E., Villar-Prados, A., Bowser, J., Broaddus, R. and Gladden, A. B. (2017). Loss of polarity alters proliferation and differentiation in low-grade endometrial cancers by disrupting Notch signaling. *PLoS ONE* **12**, e0189081.

Xian, W., Schwertfeger, K. L. and Rosen, J. M. (2007). Distinct roles of fibroblast growth factor receptor 1 and 2 in regulating cell survival and epithelial-mesenchymal transition. *Mol. Endocrinol.* **21**, 987-1000.